Effect of plasma on ultra short pulse laser material processing

Li, Chengde; Vatsya, S.R.; Nikumb, S.K.

Publisher's version / Version de l'éditeur:
https://doi.org/10.2351/1.2402521
Journal of Laser Applications, 19, 1, pp. 26-31, 2007

Effect of plasma on ultra short pulse laser material processing

Chengde Li, S.R. Vatsya and S. K. Nikumb

Integrated Manufacturing Technologies Institute, National Research

Council of Canada, London, Ontario, N6G 4X8, Canada

Abstract

Machining with high power ultra-short-pulsed lasers is becoming a preferred technique in material processing. However, the laser beam passing through a medium, e.g., air, experiences the self-focusing, Kerr effect. High intensities increased further by self-focusing cause optical breakdown of the air, generating plasma. The associated diffusion compensates for the Kerr effect but it also deforms the laser beam. In the present article, properties of the plasma columns so induced by the femtosecond laser pulses are studied, which are similar to the long filaments induced with collimated ultra short pulses. It is found that the two effects balance each other very closely for the part of the beam. Thus, placing the focal position at an appropriate position results in improved drilling and cutting, i.e., with flat bottom, parallel wall, and less dross. Theoretical calculations of the intensity profile of the optical beam propagating through air are found to be commensurate with the experimental observations.

Keywords: ultra short pulsed laser, plasma generation, laser material processing, nonlinear optics

1. Introduction

The observations of light filaments tens of meters long in air created with collimated high power ultra short laser pulses[1], has generated considerable interest in the studies of the ultra-intense laser pulse propagation in transparent media[2-12]. Such long filamentation results from a dynamic balance of the two competing nonlinear effects associated with the optical beam propagation in dielectric media. The first one is the Kerr effect, describing self-focusing of the medium resulting from higher refractive index at high intensities. The second is partially caused by the Kerr effect. High intensities are further enhanced by self-focusing to be sufficiently high to ionize the medium by multi-photon ionization and tunneling, generating plasma. The consequent photon-plasma scattering diffuses and distorts the beam in general. Existence of long filamentation indicates that the two competing effects neutralize each other almost exactly in some experimental situations, maintaining a steady profile of the optical beam, although a fragile balance. Eventually, the filamentation ends where the energy loss from ionization, inherent radiation, self-phase modulation and supercontinuum generation breaks up the process.

The investigations of the collimated and focused ultra short laser pulses interacting with gases are not only of significance to fundamental nonlinear optics, they may also lead to the understanding of phenomena such as lightning discharge in clouds[13] and ultra fast white light sources[14], as well as to applications in laser processing of materials. For the case of converging geometry, recent experiments and simulations have focused on femtosecond pulses propagating in water[15] for the purpose

of understanding the mechanism of femtosecond laser writing waveguides in fused silica[16]. In the present article, we investigate the behavior of such pulses in air for application in femtosecond laser machining in ambient air medium.

Applications of femtosecond pulses in laser material processing with converging beam propagating through air is considered undesirable for the following reason. The density of the plasma in air in the vicinity of the focal point is much higher than the plasma density in the long filaments generated by the collimated beams. The defocusing caused by plasma exceeds the self-focusing effect and the disturbance in plasma induces self-phase modulation of the laser beam. This results in a distortion of the beam profile. Therefore, femtosecond laser material processing is usually conducted in vacuum environment with associated inconvenience and expense [17,18]. It is pertinent to remark that although the plasma generation may distort the laser beam, high-energy particles in plasma, which participate in the material ablation, have positive effect in achieving better quality processed machined surfaces [19].

Beam delivery schemes of femtosecond laser radiation by inexpensive facilities at ambient pressures have been investigated recently. Doughnut shape profile produced by DOE's, have been found to produce cleaner machined surfaces [20]. Alternatively, inert gases with high ionization potential, e.g., helium, reduce the effects caused by the air breakdown with similar effects [21].

In the present article, we report the observations of filamentation consisting of high-density plasma, with converging femtosecond pulses delivered through air. The intensity in the plasma column was limited to the range of $10^{13} - 10^{14}$ W/cm^2. The energy loss for plasma generation was less than 10% for power up to 1 W. Furthermore, by placing the plasma column halfway down to the stainless steel sample surface, which is about 50 to 60 micron below the focal point, resulted in a flat bottom drilling and parallel-wall cutting. Also, the dross formation and re-deposition with this arrangement were considerably lesser than with placing the focal position below the sample surface. While an adequate modeling of the phenomena involved is quite complex and beyond the scope of this article, profile of machined surface is known to compare well with the intensity distribution of the beam. Calculations show that there is a rapid variation in the intensity profile of the beam close to the focal point. The calculated profile was found to be close to a well-peaked Gaussian distribution with little distortion, at about 50 micron below the focal point. This indicates that a cleaner machined surface should result with the material surface irradiated with this part of the beam, which is compatible with the experimental observations.

2. Experimental details

The experiments were conducted with a Clark-MXR CPA 2010 femtosecond laser, which consists of a 35 MHz SErF fiber oscillator and a chirped-pulse-amplification Ti:Sapphire regenerative amplifier. Material was processed with 150 *fs* pulses with wavelength centered at 775 *nm*, at the pulse repetition rates of 1 *kHz* and a power of 1 *W*, which corresponds to the pulse energy of 1 *mJ*. The input pulse energy was

controlled by a set of ND filters. The laser beam was collimated by a beam expander without real focus inside and expanded to fulfill the 10 *mm* clear aperture of an 8× achromatic objective (CVI Laser Co.) with NA = 0.23 and focal length of 21 *mm*. The positioning precision of the motion system used was 1 μm.

The laser system was used to process a 316 stainless steel plate. The plasma column region was imaged using a MEIJI EMZ-TR stereo-microscope with color CCD camera from the side. A stereo-microscope has long working distance and its magnification and resolution are satisfactory for this purpose. Also, the high sensitivity of CCD camera is better suited to detect faint plasma. The images were captured and analyzed by using the software Vision Gauge. To determine the impact of the plasma column generated by ultra short pulses in air on the ablation process and cutting of materials, careful observations of the laser focusing positions were made.

3. Observations

Our observations showed that the threshold pulse energy for generating visible plasma was about 50 μJ. The observed dimensions of the plasma columns with pulse energies up to about 1 mJ, with corresponding laser power of 1 W, are listed in Table 1. Because of a nonlinear dependence of ionization on the laser intensity, the transverse dimension of the ionization region is smaller than the width of the laser beam waist. The two are related by [22]

$$w_L = K^{1/2} w_{p,} \tag{1}$$

where w_L is the beam waist, w_p is the diameter of the plasma column and K is the Keldysh exponent. The value of the Keldysh exponent for P=140μJ, w_p = 14μm, w_L = 43μm, and the intensity I = 6.3×10^{13} W/cm^2 is given by K = 9.6[23] As the calculated pulse energy increases from 50 μJ to about 1mJ, the intensity in the vicinity of the focal point varies in the range of $10^{13} - 10^{14}$ W/cm^2, which is comparable with the intensity for the case of filamentation occurring in collimated ultrashort pulse delivery in air[10]. Initially, an ultrafast laser pulse generates electrons exclusively through multiphoton ionization due to the fact that the duration of the pulse is short compared to the average collision times, followed by avalanche or the cascade ionization. As the electron density reaches the critical value, high density plasma is created due to the resulting air breakdown. Photon-plasma defocuses the laser beam reducing the local intensity, which is commensurate with the above observation.

Figure 1 shows the plasma columns generated with laser power of 140 mW to 980mW. The columns have symmetrical shapes with well-defined boundaries. The dashed line indicates the location of the focal point. According to the moving-focus model[13] the focal point Z_{fR} should sweep back and forth along the propagation axis z but within a distance limited by the focal length f of the lens according to $Z_{fR} = (1/z_f + 1/f)^{-1}$, with z_f is given by[24]

$$Z_f(t) \approx \frac{0.367k\ w_L^2}{\{P[t - \frac{z_f(t)}{v_g}]P_2\}^{1/2} - 0.852} \qquad (2)$$

where k is the wave vector, a is the beam waist, P_2 is the critical power, and v_g is the group velocity. To determine the energy consumed in forming the plasma column, laser power in front of the columns and behind them was measured. The observed energy loss is plotted in Figure 2, which shows that the maximum loss for laser power up to 1 W is less than 10%. These results are in agreement with the total energy of about 7% contained in the long filaments [3], where there was no optical breakdown. This indicates that the energy loss observed in the present experiments is due mainly to the generation of plasma.

Figures 3(a) to 3(c), show the plasma column produced by the air breakdown moving and merging with the plasma plume produced by laser ablation. The plume is seen to expand transversally as these two plasmas merge together. The high temperature air plasma column can transfer energy to the particles in the ablation plume. Since the low energy plum could fall back to the irradiated surface, this has an effect to reduce dross and re-deposition around the ablation site.

Figure 4 compares the quality of the holes drilled with 150 *fs* and 40 *ns* laser pulses. The figure shows the 1000× SEM photographs of the holes drilled by 2000 shots with laser power of 100 mW at pulse repetition rate of 1 kHz, in each case. The femtosecond pulse generated a plasma column of length of about 70 μm and 10 μm in diameter. Nanosecond pulse does not generate any visible plasma. This figure also shows the effect of the location of the focal point on the quality of the processed surface. For Figures 4 (a) and (b) plasma column was halfway down the sample surface as indicated.

In general, the nanosecond pulses produce melt and dross. In case of the femtosecond pulses, there is little melt and dross resulting in cleaner fabricated surface. Quality of the surface was found to be optimal when the focal point is a small distance above the surface, producing holes with steep walls, flat glossy bottom surface and well-defined periphery.

It has been reported that air breakdown in focal vicinity could deform the wavefront of the ultrashort pulses resulting in deviation of the transverse mode from a Gaussian distribution [9]. Furthermore, self-phase modulation forms a ring structure in the beam profile [25,26]. These observations were made somewhere behind the focal region, since it is impossible to place a detector in the focal region directly. Our monitoring of the intensity distribution behind the focal point indicated that the energy about the center of the laser beam was considerably depleted due to generation of the plasma for input laser powers greater than 500 mW, resulting in the transverse intensity profile with a donut structure.

According to a recent study on the time-resolved visible spectroscopy of plasma produced by the breakdown of air using femtosecond pulses, the emission from the plasma is initially dominated by N_2 molecular lines, then followed by the continuum emission with a growth time of about 3 *ns* and a decay time of about 30 *ns* [23]. Atomic lines of N_2 and O_2 emerge from the decay of the continuum and last up to 1 μs. Thus, initially the ultra short laser irradiation ablates the materials from the sample. Then, the particles that have not been ionized in the ablation plume are heated by the long

lasting air plasma resulting in a reduction in the dross around holes observed in Figure 4 (a) and (b).

Figure 5 shows a channel cut at the laser power of 28 mW with focal position 60 μm 60 μm under the sample surface, resulting in funnel shaped cross section. The depth of the cut is about 70 μm and the width is 16 μm. The irradiation fluence is estimated as 13.6 J/cm^2. Reconsolidation of the materials is noticeable on the ramping edge of the cut. Figure 6 shows a channel cut with focal position on the sample surface. The wedge-shaped channel is 8 μm in width on the surface and 90 μm in depth. The higher irradiation fluence of about 54.7 J/cm^2 improved the shape of the cut. However, reconsolidation still made the edges and walls of the channel ripple. Figure 7 shows a channel cut by a laser power of 165 mW with the focal point about 60 μm above the sample surface. This produced a 100 μm long plasma column due to air breakdown. The width of the channel is 35 μm and the depth is about 160 μm. The cutting quality is improved considerably. There is no dross inside the channel and no reconsolidation along the edges, and the wall angle is approximately 90°.

4. Optical beam profile

While a complete modeling of the laser-material interaction during ablation involves a number of complex phenomena, qualitative inferences can be drawn from the intensity distribution in the beam about the ablation region, as the fabricated surface conforms to a significant extent to the beam profile. Propagation of an optical beam through a medium is described by the following nonlinear Schödinger type equation [21, 26, 27]:

$$\frac{\partial A}{\partial z} - \left[\frac{i}{2k}\left(\frac{\partial^2}{\partial x^2} + \frac{\partial^2}{\partial y^2}\right) + in_2 k\,|A|^2 - \frac{kN_e}{2N_c}\right] A = 0 \qquad (3)$$

where λ is the wavelength, $k = 2\pi/\lambda$ is the wave number and the intensity $I = |A|^2$. The refractive index $n(I) = (n_0 + n_2 I)$, where n_2 is the optical Kerr coefficient. The electron density N_e follows the rate equation,

$$\frac{dN_e}{dt} = N_0 R$$

where N_0 is the number density of the neutral gas molecules. The critical plasma density N_c is defined in terms of the speed of light, the electron charge and the electron mass by $N_c = [(k^2 m_e c^2)/(4\pi e^2)]$ in standard notation, and the ionization rate is given by $R = (0.2\sigma_{O_2}|A|^{2n} + 0.8\sigma_{N_2}|A|^{2m})$, where σ_{O_2}, σ_{N_2}, n, m are the scattering cross-sections and effective multi-photon numbers respectively for oxygen and nitrogen, which are determined experimentally[7]. The coefficients 0.2 and 0.8 are used on the assumption that air constitutes of 20% oxygen and 80% nitrogen.

For a radially symmetric system, Eq. (3) can be expressed as

$$\frac{\partial A(r,t,z)}{\partial z} - \left[\frac{i}{2k}\left(\frac{\partial^2}{\partial r^2} + \frac{1}{r}\frac{\partial}{\partial r}\right) + in_2 k\,|A|^2 - \frac{2\pi e^2 N_e}{km_e c^2}\right] A(r,t,z) = 0 \qquad (4)$$

With lens placed at the beam waist, the boundary condition is given by

$$A(r,t,0) = A_0 \exp[-(r^2/w_0^2 + \tau^2/\tau_p^2) - ikr^2/2f],$$

where A_0, w_0, τ_p f and $\tau = (t - z/c)$ are the maximum amplitude, radius of the beam-waist, pulse-width, focal length of the lens and the retarded time, respectively. Commonly used methods to solve Eq. (4) are the finite difference methods[26], which tend to accumulate round off errors and the fast Fourier transform [27], which are inconvenient for applications in cases of converging beams. For accuracy, we have used a method based on the eigenfunction expansion described below, which is better suited for the cylindrical coordinate system. In all numerical methods, it is necessary to use a finite interval, which is justified for the beam intensity diminishes to close to zero at some finite value of $r = r_{\max}$. Therefore, the r coordinate will be restricted to the interval $[0, r_{\max}]$. Eq. (4) can be expressed in compressed notation as

$$\frac{\partial A}{\partial z} - \left[\frac{i}{2k} B + V(|A|)\right] A = 0 \qquad (5)$$

where B denotes the differential operator with respect to r, and V denotes the remaining two terms. The operator B admits the spectral representation:

$$B = -\sum_{\mu=0}^{\infty} \lambda_\mu^2 \, p_\mu$$

where the projection operator p_μ is defined by $p_\mu u = \phi_\mu(\phi_\mu, u)$ with the scalar product given by

$$(u, w) = \int_0^{r_{\max}} dr \, r \, u(r) w(r) .$$

Here $(-\lambda_\mu^2)$ and ϕ_μ are the eigenvalues and the corresponding normalized eigenvectors of B, respectively. The eigenvalues λ_μ are the zeros of the zero order Bessel function and

$$\phi_\mu = [\sqrt{2} J_0(\lambda_\mu r)/(r_{max} J_1(\lambda_\mu r_{max}))],$$

where $J_0(\lambda_\mu r)$ and $J_1(\lambda_\mu r)$ are the Bessel functions of zero and first order respectively. Consequently, the solution of Eq. (5) is given by

$$\begin{aligned} A(z) &= \exp[\frac{i}{2k} Bz] \left(A(z=0) + \int_0^z dz' \exp[-\frac{i}{2k} Bz'] V(z') A(z') \right) \\ &= \sum_{\mu=0}^{\infty} \phi_\mu \exp\left[\frac{-i\lambda_\mu^2}{2k} z \right] \left((\phi_\mu, A(z=0)) + \int_0^z dz' \exp[\frac{i\lambda_\mu^2}{2k} z'] (\phi_\mu, V(z') A(z')) \right) \end{aligned} , \quad (6)$$

with values of $(\phi_\mu, A(z=0))$ determined by

$$(\phi_\mu, A(z=0)) = \frac{\sqrt{2} A_0}{r_{max} J_1(\lambda_\mu r_{max})} \int_0^{r_{max}} dr\, J_0(\lambda_\mu r) \exp[-(r^2/w_0^2 + \tau^2/\tau_p^2) - ikr^2/2f].$$

Numerical integrations require some care in case of the rapidly oscillating functions as is the case here. Suitable methods were used to reduce the difficulties associated with the rapid oscillations and their accuracy was assured by comparing the numerical values with the analytically calculated values of $(\phi_\mu, A(z=0))$ as an infinite series. The integral in Eq. (6) was approximated as

$$T(z+\Delta z) = \int_0^{z+\Delta z} dz' \exp[\frac{i}{2k}\lambda_\mu^2 z'] \, (\phi_\mu, V(z')A(z'))$$

$$; \quad T(z) + (\phi_\mu, V(z)A(z)) \int_z^{z+\Delta z} dz' \exp[\frac{i}{2k}\lambda_\mu^2 z'] \tag{7}$$

$$= T(z) - \frac{2ik}{\lambda_\mu^2}(\phi_\mu, V(z)A(z)) \exp[\frac{i}{2k}\lambda_\mu^2 z] \left(\exp[\frac{i}{2k}\lambda_\mu^2 \Delta z] - 1 \right)$$

which can then be evaluated at all z points starting with the zero where its value is equal to zero. This approximation reduces the difficulties created by the oscillations. It is necessary to truncate the sum at some finite value of μ. In the present calculations, five to seven terms were found to be sufficient.

Numerical results for the input parameters corresponding to the present experimental results are shown in Figure 8. The fluence normalized with respect to the peak input fluence is plotted against the radial distance in units of the beam radius, at the focal point, 50 μm below the focal point and 60 μm below the focal point. At the focal point, the fluence profile deviates from the Gaussian for the values of the radial coordinate higher than about 1.5 times the half beam-width, where it is sufficiently high to ablate the material or cause damage. Thus, the ablated crater is expected to be deformed about the boundary. This conclusion is in agreement with the observations of Figures. 4 and 6. If the material surface is placed below the focal point, the profile gets closer to the Gaussian. In our experimentation, the most desirable profile was found at about 50 μm below the focal point where the profile is well shaped and the intensity is well below threshold outside about equal to the half beam-width. Thus, placing the

material about 50 μm below the focal point should result in a cleaner cut of about half width radius. Experimentally, the cleanest cut was found to be at about 60 μm as indicated in Figures 4 and 7. In view of the uncertainties in the experimental parameters and the measurements coupled with the modeling and numerical approximations, this is an excellent agreement.

The calculated values are neither symmetric about the focal point, nor about the 50 μm mark, but the values at 40 μm below the focal point were found to be close to the ones at 60 μm below. The beam shape above the focal point was found to be close to the Gausian but with low intensity. As a result of low intensity, there is little direct ablation, instead considerable amount of melt should form. Also, for lack of sufficient energy for transfer to plasma, more re-deposition results. This observation is also compatible with the results of Figures 4 and 5.

5. Concluding remarks

In the present article, the observations of short filaments of the plasma columns induced by the femtosecond laser breakdown of air in the focal region are reported. These columns are found to have properties similar the long filaments induced with collimated ultra short pulses, in terms of the intensity in the plasma columns and the energy consumed in producing them. It is shown that the flat-top intensity distribution in the cross section of the plasma column can be exploited in drilling and cutting of stainless steel with flat bottom and parallel wall, by placing the plasma column halfway down to the sample surface. Appropriate location of the plasma column also increases the energy

transferred to the plasma plum rising from the ablated material, which results in a decrease in re-deposition and dross on the periphery of the processed surface. Numerical calculations of the intensity distribution in the optical beam propagating through air are found to be in a qualitative agreement with the experimental observations.

Acknowledgements

The authors are grateful to M. Islam, Director, Production Technology Research, for his support, and Hugo Reshef, Craig Dinkel and Mike Meinert for their technical assistance.

References

[1] A. Braun, G. Korn, X. Liu, D. Du, J. Squier, and G. Mourou, Opt. Lett. **20** (1995) 73.

[2] E.T.J. Nibbering, P.F.Curley, G.Grillon, B.S.Prade, M.A.Franco, F.Salin, and A. Mysyrowicz, Opt. Lett. **21** (1996) 62.

[3] A. Brodeur, C.Y.Chien, F. A. Ilkov, S. L. Chin, O. G. Kosareva and V. P. Kandidov, Opt. Lett. **22**,(1997) 304.

[4] H. R. Lange, G. Grillon, J. F. Ripoche, M. A. Franco, B. Lamouroux, B. S. Prade, A. Mysyrowicz, E. T. J. Nibbering, and A. Chiron, Opt. Lett. **23** (1998) 120.

[5] M. Mlejnek, E. M. Wright, and J.V.Moloney, Opt. Lett., **23** (1988) 382.

[6] A. Brodeur and S. L. Chin, Phys. Rev. Lett., **80** (1998) 4406.

[7] A. Talebpour, J. Yang, and S. L. Chin, Opt. Commun., **163** (1999) 29.

[8] A. Talebpour, M. A. Fattah, and S. L. Chin, Opt. Commun. **183** (2000) 479.

[9] J. Schwarz, P. Rambo, J. C. Diels, M. Kolesik, E. M. Wright, J. V. Moloney, Opt. Commun. **180** (2000) 383.

[10] J. Kasparian, R. Sauerbrey, S. L. Chin, Appl. Phys. B **71** (2000) 877.

[11] B. Tzortzakis, L. Berge, A. Couairon, M. Franco, B. Prade, and A. Mysyrowicz, Phys. Rev. Lett., **86** (2001) 5470.

[12] A. Couairon and L. Berge, Phys. Rev. Lett., **88** (2002) 135003-1.

[13] X. M. Zhao, J. C. Diels, C. Y. Wang and J. M. Elizondo, IEEE J. Quan. Electron., **31** (1995) 599.

[14] R. R. Alfano, Ed., The Supercontinuum Laser Source, Springer, New York, 1989.

[15] W. Liu, O. Kosareva, I. S. Golubtsov, A. Iwasaki, A. Becker, V. P. Kandidov, S. L. Chin, Appl. Phy. B **76** (2003) 215.

[16] S. Tzortzalis, L. Sudrie, M. Franco, B. Prade, and A. Mysyrowicz, Phys. Rev. Lett., 87 (2001) 213902-1.

[17] M. Meunier, B. Fisette, A. Houle, A. V. Kabashin, S. V. Broude, P. Miller, SPIE USE, Vol. 6 (2003) 4978.

[18] C. Momma, S. Nolte, G.Kamlage, F. von Almensleben, A. Tunnermann, Appl. Phys, A **67** (1998) 517.

[19] C. Li and S. K. Nikumb, Appl. Opt., **42** (2003) 2383.

[20] S. Preuss, A. Demchuk, M. Stuke, Appl. Phys. A **61** (1995) 33.

[21] J. Sun and J.P. Longtin, J. Appl. Phys., **89** (2001) 8219.

[22] F. Vidal, D. Comtois, C. Y. Chien, A. Desparois, B. La Fontaine, T. W. Johnson, J. C. Kieffer, H. P. Mercure, H. Pepin, and F.A. Rizk, IEEE Trans. Plasma Sci. **28** (2000) 418.

[23] F. Martin, R. Mawassi, F. Vidal, I. Gallimberti, D. Comtois, H. Pepin, J. C. Kieffer, and H. P. Mercure, Appl. Spectro., **56** (2002) 1444.

[24] J. H. Marburger, Prog. Quantum Eletron. **4** (1975) 35.

[25] S.C. Rae, Opt. Commun., **104** (1994) 330.

[26] S. L. Chin, N. Aközbek, A. Proulx, S. Petit and C. M. Bowden, Opt. Commun., 188 (2001) 181-186

[27] D. Subbarao, H. Singh, R. Uma and S. Bhaskar, J. Plasma Phys., 61 (1999) 449-467.

Captions

Table 1. Correlation of the dimensions of the plasma columns and the laser power.

Figure 1. Calibrated optical microscopic images of the plasma columns in the focal vicinity generated with 150 fs pulses.

Figure 2. Energy loss due to femtosecond pulses breakdown of air.

Figure 3. Plasma density variarion during merger of the column due to air breakdown and the ablation plume.

Figure 4. Comparison of the holes drilled with femtosecond pulses (fs) and with nanosecond pulses (ns). Relative location of the focal point is shown to the left of the craters.

Figure 5. Channel cut with focal position below the sample surface.

Figure 6. Channel cut with focal position on the sample surface

Figure 7. Channel cut with focal point above the sample surface.

Figure. 8. Normalized fluence profile at the focal point (0 μm), 50 μm below the focal point (50 μm) and 60 μm below the focal point (60 μm).

Table 1

Laser Power (mW)	50	80	120	140	160	260	380	550	980
Diameter of Plasma Column (μm)	-	7	11	14	18	28	42	60	88
Length of Plasma Column (μm)	-	55	72	81	92	142	174	227	294

C. Li, S. R. Vatsya and S. K. Nikumb

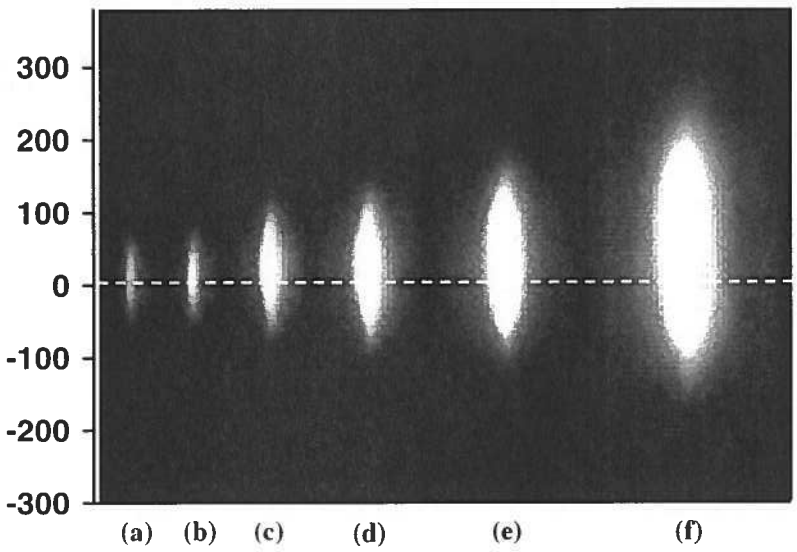

Figure 1.

C. Li, S. R. Vatsya and S. K. Nikumb

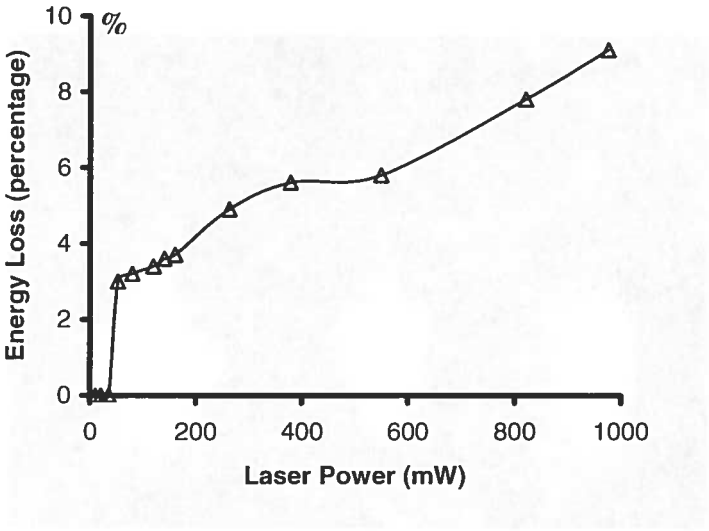

Figure 2.

C. Li, S. R. Vatsya and S. K. Nikumb

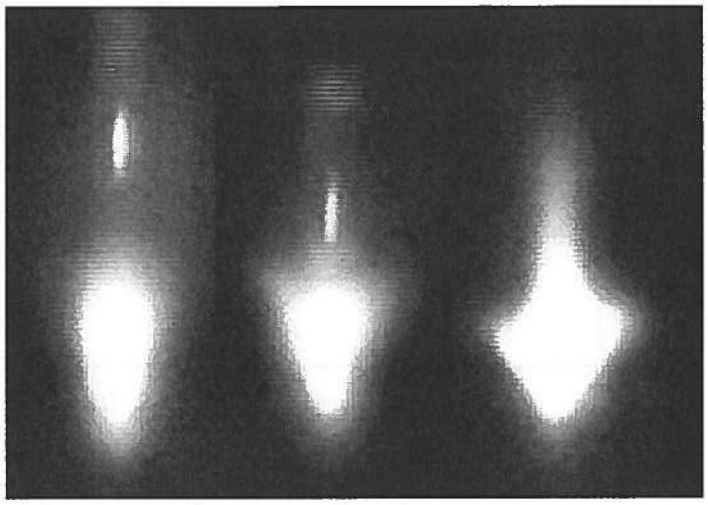

(a) (b) (c)

Figure 3.

C. Li, S. R. Vatsya and S. K. Nikumb

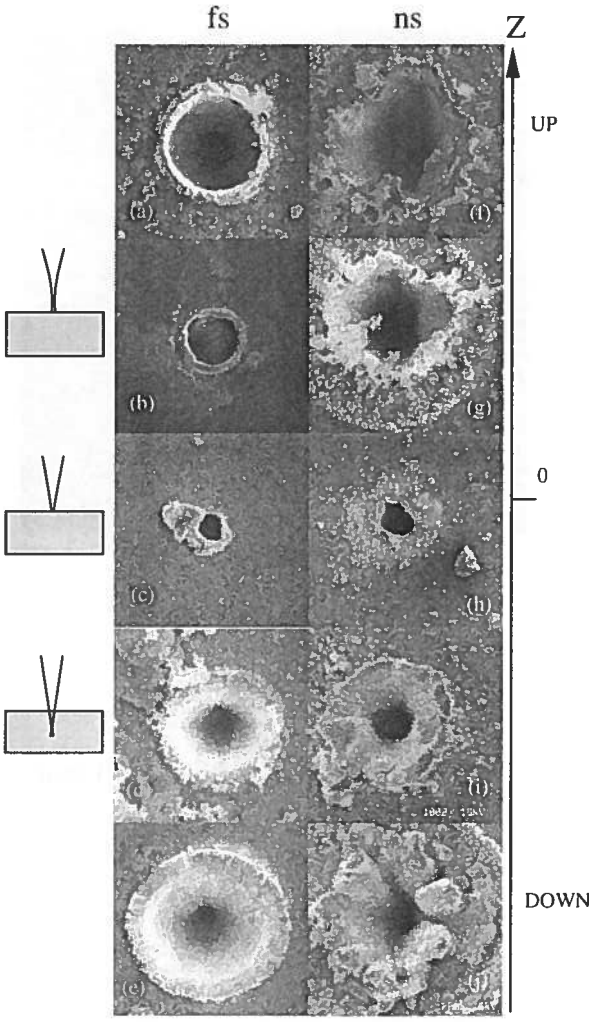

Figure 4.

C. Li, S. R. Vatsya and S. K. Nikumb

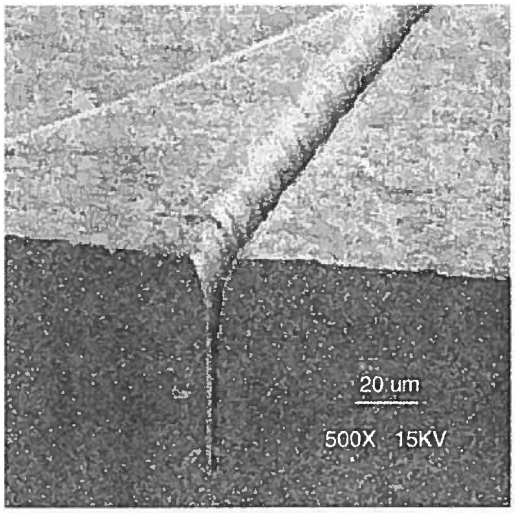

Figure 5.

C. Li, S. R. Vatsya and S. K. Nikumb

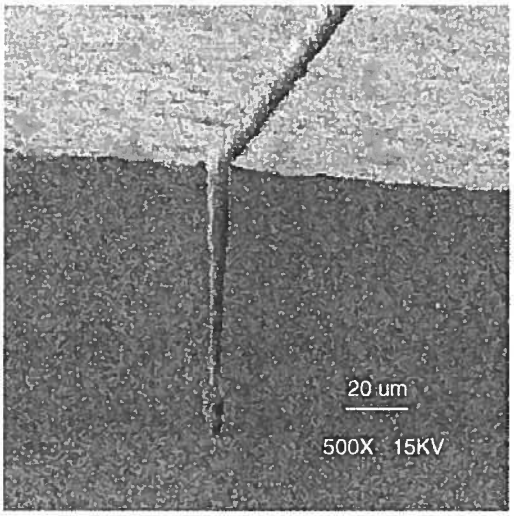

Figure 6.

C. Li, S. R. Vatsya and S. K. Nikumb

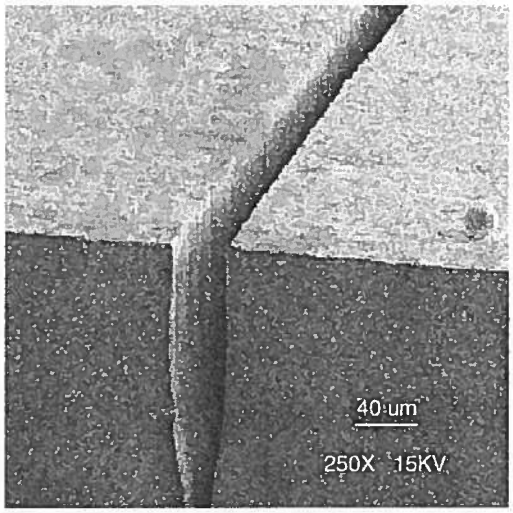

Figure 7.

C. Li, S. R. Vatsya and S. K. Nikumb

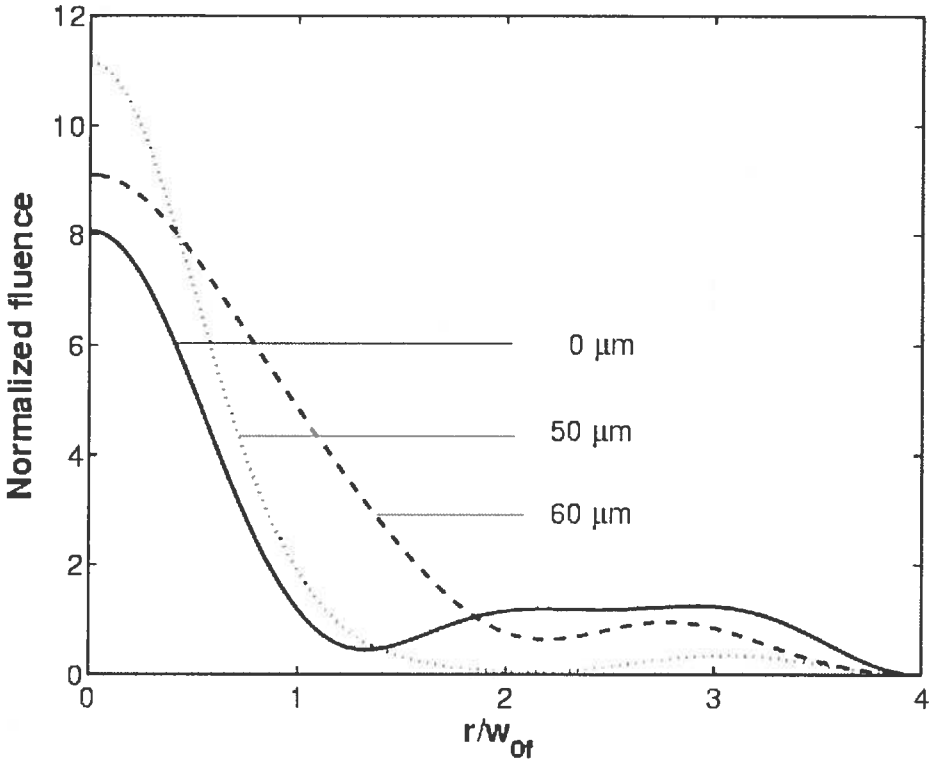

Figure 8.

C. Li, S. R. Vatsya and S. K. Nikumb